ARTICLE

Near-Field Spectroscopy of Broadband Emissions from γ-Al$_2$O$_3$ Nanocrystals in Cr-Doped Double-Clad Fibers

Chien-Chih Lai,[†] Shih-Chang Wang,[†] Yen-Sheng Lin,[‡] Ting-Hao Chen,[†] and Sheng-Lung Huang[*,†,§]

[†]Institute of Photonics and Optoelectronics and [§]Department of Electrical Engineering, National Taiwan University, Taipei 106, Taiwan
[‡]Department of Electronic Engineering, I-Shou University, Kaohsiung 840, Taiwan

S *Supporting Information*

ABSTRACT: Embedded nanocrystals (NCs) of γ-Al$_2$O$_3$ in SiO$_2$ matrixes of Cr-doped double-clad fibers (CDFs) were fabricated by the codrawing laser-heated pedestal growth technique. The spatially resolved broadband emissions of these NCs were examined as a function of NC morphology and distribution by near-field scanning optical microscopy. Comparison of the measured emissions with crystal-field ligands together with careful examination of the NC morphologies by high-resolution transmission electron microscopy confirmed this broadband emission as being an effect of nanotwinning and the Cr^{3+}−Cr^{6+}

redox reaction. The impact of nanotwinning on the relative strength and emission wavelength of Cr^{3+} and Cr^{6+} is potentially beneficial for broadband emission at visible wavelengths to achieve ultra-high-resolution optical coherence tomography (OCT). As is evident from the near-field spectrum, a 1.2-μm axial resolution in air for OCT can be achieved with a CDF with a 165-nm bandwidth centered at 690 nm.
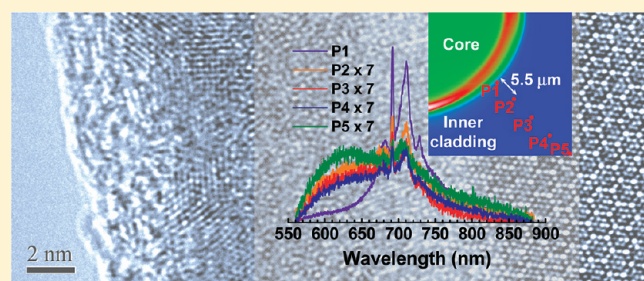
1. INTRODUCTION

Broadband emissions at visible wavelengths are desirable for optical coherence tomography (OCT) systems, which have shown huge potential for offering in vivo three-dimensional tomographic imaging of biotissues with cellular resolution.[1] The axial resolution is inversely proportional to the bandwidth of the light source and is proportional to the square of the center wavelength. A fiber-based broadband light source can provide a compact and robust alternative to existing OCT light sources, such as multiplexed superluminescent diodes, femtosecond lasers, and the photonic-crystal-fiber-generated supercontinuum.[2−4] Transition-metal-doped fibers can offer broadband emissions based on unscreened electronic configurations. It is well-known that the spectral characteristics of transition-metal dopants are influenced more significantly in glasses than in crystals because there are a variety of sites in glasses for active ions to reside. Therefore, it is advantageous to use noncrystalline fiber light sources with short wavelengths to enhance imaging resolution.

As the size of particles decreases down to the nanoscale, size effects can appear. Semiconductor nanocrystals (NCs) exhibit a wide range of optical and electrical properties because of the quantum confinement effect.[5] For insulators, however, it is much harder to observe the quantum confinement effect, because their electronic states are strongly localized.[6] Nevertheless, Mercier et al. claimed that a significant increase in bandgap energy was observed in Ce^{3+}:Y$_2$O$_3$ insulators ranging from 3 to 40 nm.[7] In the present case of transition-metal-doped insulators, the optical properties of the transition-metal ions are quite sensitive to the local environment because of their open-shell d−d electronic

transitions. As a result, the quantum confinement effect manifests itself in the form of strong electron−electron coulomb interactions. Although the detailed mechanism has yet to be explained, careful examination of about 150 NCs revealed that there was no size effect. The luminescence difference in Cr^{3+}:γ-Al$_2$O$_3$ NC could possibly be due to the local environment of the emitters.

Broadband emission materials, especially Cr-doped crystals and glasses, have recently attracted great interest for practical applications in telecommunications.[8] In particular, glasses doped with transition-metal NCs are promising for broadband applications in OCT systems. However, most previous studies were performed on the fabrication and characterization of NC-doped materials.[9−12] Although the formation mechanism of the NC structure is crucial for determining optical properties, direct observations of the evolution of spectroscopy dependent on NC morphology have rarely been reported, particularly for fibers. Twinning, a common defect frequently observed in face-centered-cubic-structured NCs, has been found to strongly influence optical properties. However, nanotwinnings are difficult to investigate because they form rather slowly and through a transient process. This makes it more difficult to develop a clear understanding of the corresponding formation mechanism. To further unravel the mechanism that leads to broadband emission, in this study, Cr-doped double-clad fibers (CDFs) with different sizes of γ-Al$_2$O$_3$ NCs embedded in the amorphous SiO$_2$ matrixes were fabricated by the

codrawing laser-heated pedestal growth (CDLHPG) technique. Through measurements of the nanostructure and nanospectroscopy, a plausible elucidation of the formation mechanism of twinned NCs and large NCs is provided. The effect of nanotwinning on the relative strength and emission wavelength of Cr^{3+} and Cr^{6+} to produce a bandwidth of 165 nm at visible wavelengths was investigated.

2. EXPERIMENTAL SECTION

2.1. Crystal Fiber Growth and Nanostructural Characterization. A Cr:YAG single-crystal fiber with a core diameter of 68 μm was initially prepared from a 0.5 mol % Cr-doped and $\langle 111 \rangle$-oriented source rod. For the CDLHPG process, the fiber was then inserted into a fused silica capillary with inner and outer diameters of 76 and 320 μm, respectively. The core diameter depends on the speed of growth and the CO_2 laser power utilized in the CDLHPG system. In this study, a drawing speed of 30 mm/min was applied to form a 54-μm-diameter core. To examine the relationship between the morphology and the near-field spectroscopy of twinned γ-Al_2O_3 NCs with various sizes, a high-resolution transmission electron microscope (HRTEM, FEI Tecnai G^2 F20 FEG-TEM) and a modified multipump near-field scanning optical microscope (NSOM, NT-MDT NTEGRA Spectra) were employed. (See the Supporting Information for a description of the multipump NSOM.) The structures of the γ-Al_2O_3 NCs and clusters were further identified by 2-nm-beamsize selected-area electron diffraction (SAED) and energy-dispersive X-ray (EDX) analyses. The corresponding lattice images together with inverse Fourier transforms were employed to characterize the coherent (hkl)-twinned planes. Lattice image simulations based on the multislice method were performed with the MacTempas software package for comparison with the experimentally obtained images. Atomic image processing was performed using the Gatan Digital-Micrograph software. HRTEM images were compared with diffractions using the processed image to confirm the local orientations of twinned and untwinned γ-Al_2O_3 NCs.

2.2. Near-Field Spectroscopic Characterization. Spatially resolved spectroscopy was performed by 532-nm excitation to analyze NCs and clusters in the CDF. The excitation entered the spectrometer through a single-mode fiber, followed by a laser-line filter and a beam expander. Then, it was reflected by an edge filter, incident on the filter turret before passing into an inverted optical microscope (IX70, Olympus) through a 100× objective (NA = 0.95, Olympus) in collection mode or entering a fiber coupler in transmission mode. Thus, by simply rotating the filter turret, the instrument could easily be switched between the different modes. The tip−sample distance of the near-field fiber probe with a 30-nm aperture size was controlled by the shear force mechanism through a feedback system. Near-field fluorescence signals were collected through an Al-coated tapered optical fiber (630-HP, Nufern) and detected with a thermoelectrically cooled charge-coupled detector (BV401A-BV, ANDOR) at −50 °C. The corresponding near-field images were obtained by scanning the specimen with an x, y stage equipped with a closed-loop feedback system. The HRTEM results were compared with those measured on a spatially resolved NSOM. Finally, the near-field spectroscopic characteristics of the NCs and clusters in the CDF were resolved.

3. RESULTS AND DISCUSSION

3.1. Nanostructure at the Core/Inner-Clad Interface. To understand the formation mechanism of the NCs and the effect
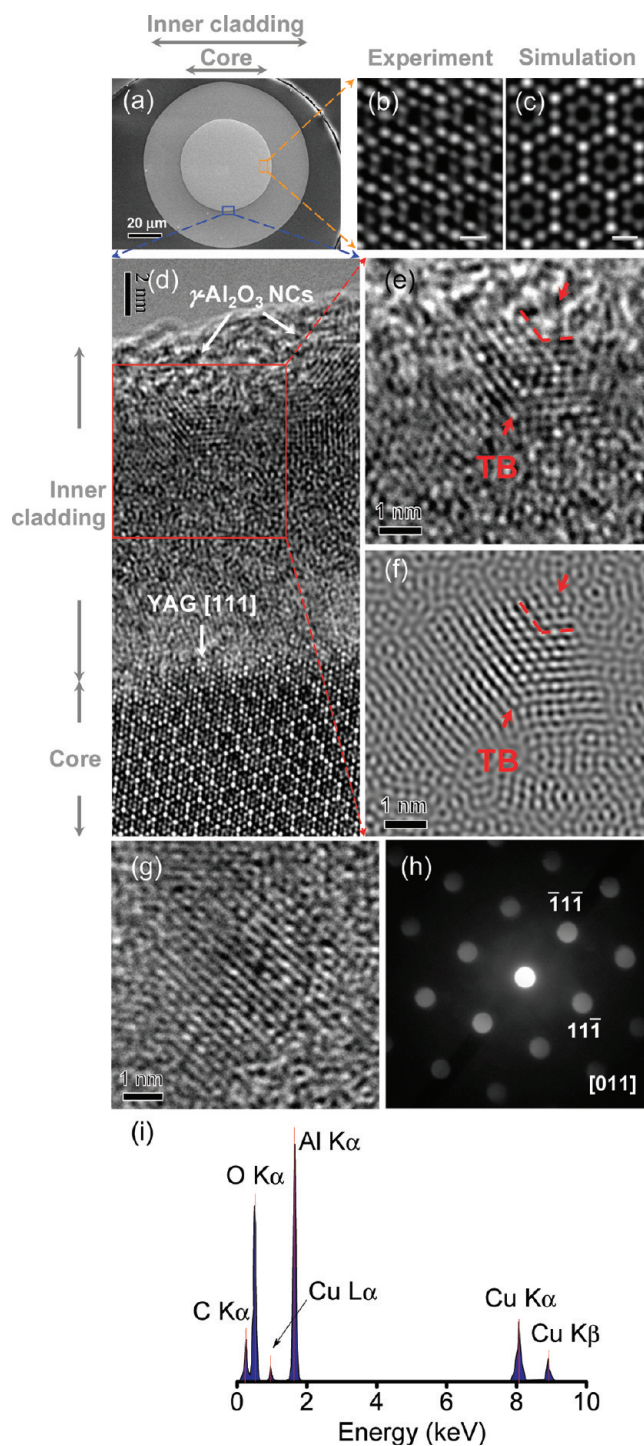

Figure 1. (a) End face image of a Cr-doped double-clad fiber (CDF); atomic-scale images of the (b,c) core and (d) core/inner-clad interface, revealing the embedded γ-Al_2O_3 NCs in SiO_2 matrixes; and two representative HRTEM images of (e) nanotwinned and (g) untwinned NCs. The TB was identified by the inverse Fourier transform shown in f. (h) Nanobeam SAED and (i) EDX analysis, indicating that the untwinned γ-Al_2O_3 NC has Al and O peaks with negligible impurities. The thickness and defocus employed in part b were 6 nm and 23 Å, respectively. Scale bars in b and c are both 5 Å.

of the nanotwinned NCs on the spectroscopic properties, a comprehensive investigation of the nanostructure at the

20290

dx.doi.org/10.1021/jp203901t |*J. Phys. Chem. C* 2011, 115, 20289–20294

core/inner-clad interface of the CDF was performed by HRTEM. Figure 1 shows HRTEM images of the core and core/inner-clad interface of the CDF. The finely polished end face of the CDF shown in Figure 1a has core and inner-cladding diameters of 54 and 98 μm, respectively. The lower part of Figure 1d presents the uniform lattice structure with no evident defects, indicating that the Cr:YAG core has high crystallinity, as confirmed by the simulated HRTEM image (Figure 1c) that optimally fits the experimental image (Figure 1b). The thickness and defocus length employed in the lattice simulation were 6 nm and 23 Å, respectively. From the electron-probe microanalyzer (EPMA) measurement of the CDF, it can be seen that the major composition in the interface between the core and inner cladding is very sharp. It is, therefore, speculated that the core does not melt. This indicates that the stoichiometry of the core YAG remains intact. The upper part of Figure 1d is a composite of γ-Al$_2$O$_3$ NCs embedded in the amorphous SiO$_2$ matrixes as a result of YAG/SiO$_2$ interdiffusion. The γ-Al$_2$O$_3$ occurs in nanosize particles because of its lower surface energy but higher entropy than α-Al$_2$O$_3$.[13] The spherical shape of these small γ-Al$_2$O$_3$ NCs suggests that they were simply crystallized from the YAG/SiO$_2$ interdiffusion melt. Furthermore, HRTEM examination clearly shows that there are two types of dominant γ-Al$_2$O$_3$ NCs, each with the same diameter of around 3 nm. These were twinned and untwinned NCs, as revealed in parts e and g, respectively, of Figure 1. Figure 1f shows the corresponding inverse Fourier transforms of Figure 1e with a marked twinning boundary (TB). The twinned NCs were generated by interdiffusion followed by high-temperature annealing and rapid cooling. It is noteworthy that Figure 1e,f shows the initial stage of the NC formation process. The TB serves as the NC/NC plane, further migrating toward the smaller NC (right part of TB) through Brownian motion to coalesce and rotating to reach a low surface energy. This leads to a coherent−NC/NC plane, that is, a single NC without twinning, as shown in Figure 1g.

Al$_2$O$_3$ polymorphs have attracted great interest because of their use in a wide range of applications. However, the underlying mechanisms of nanosized Al$_2$O$_3$ formation through interdiffusion, in particular, the evolution of the morphology and the coalescence of aggregated NCs associated with optical properties, are not clear. The formation of these NCs through an interdiffusion process followed by rapid cooling is of concern because of its potential use in biophotonic applications. At this stage, one can estimate the corresponding cooling rate u related to the NC diameter D and the temperature of the crystallized NC T_{NC} and the ambient temperature T_{amb}, together with the physical parameters of bulk Al$_2$O$_3$, through the expression $u = 6\varepsilon\sigma(T_{NC}^4 - T_{amb}^4)(D\rho C_p)^{-1}$.[14−20] ε, σ, ρ, and C_p are the radiant emissivity, Stefan−Boltzmann constant, material density, and heat capacity, respectively. The parameter values used for T_{NC}, T_{amb}, ε, σ, ρ, and C_p for γ-Al$_2$O$_3$ are 2327 K, 298 K, 0.69, 5.67×10^{-8} W m^{-2} K^{-4}, 3.67 g cm^{-3}, and 0.811 J g^{-1} K^{-1}, respectively. The cooling rate of these 3-nm-sized γ-Al$_2$O$_3$ NCs fabricated by the CDLHPG technique was found to be ∼8×10^8 K/s, which is comparable to the value of 10^9 K/s obtained for 10-nm-sized TiO$_2$ NCs by pulsed laser ablation.[21] The high cooling rate indicates a very large stress at high temperature, which results in the dense polymorphs of the NCs.

In addition, EDX analysis (Figure 1i) demonstrates that the γ-Al$_2$O$_3$ NCs have Al and O peaks with negligible impurities, whereas the Cu counts are from the supporting copper grid. As confirmed by nanobeam diffraction and EDX analysis, the
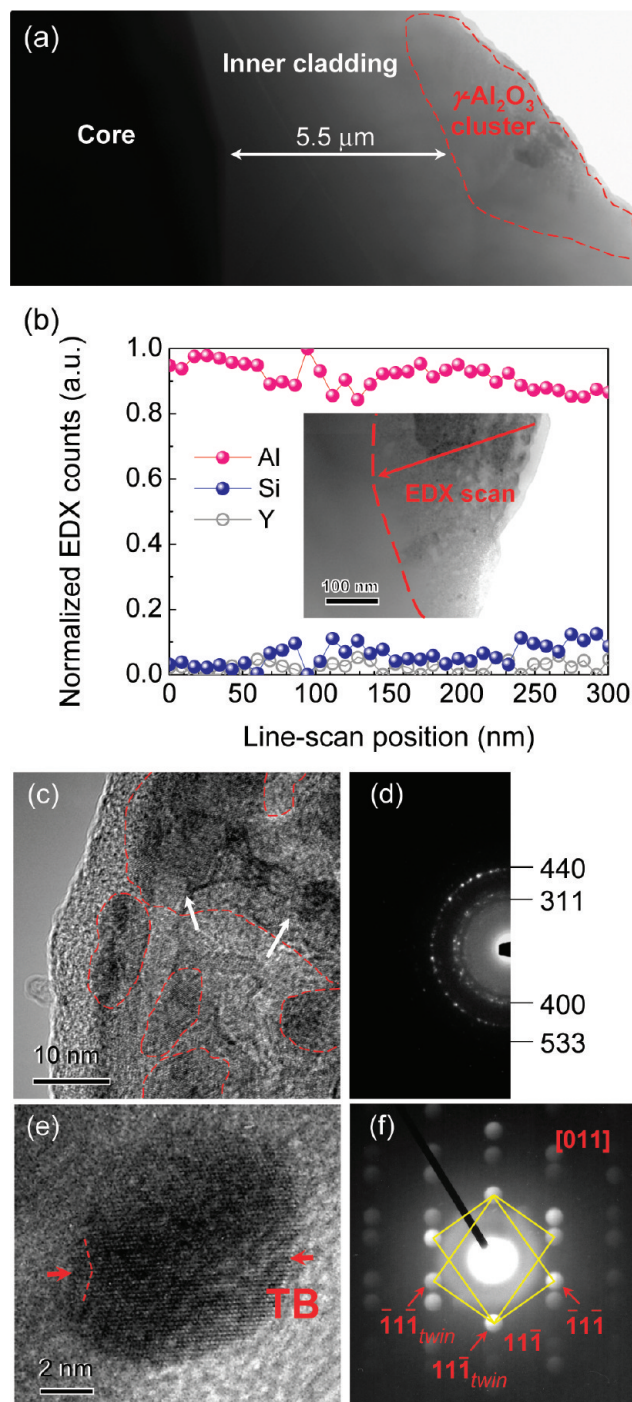

Figure 2. (a) Micrometer-sized γ-Al$_2$O$_3$ cluster (with boundaries shown by red dashed lines) formed away from the core/inner-clad interface. (b) Line-scan EDX showing an Al-rich area. Inset in b: enlarged image of the cluster in a, with an arrow showing the EDX scanning direction. (c) Magnified HRTEM image of the cluster in part a and (d) the corresponding SAED pattern. (e) HRTEM image of a 10-nm-sized γ-Al$_2$O$_3$ NC with a coherent (111) twinned plane, as evidenced in (f) the [011]-zone nanobeam SAED pattern.

identity of the NCs was also carefully verified by the SAED pattern taken from a large area to include enough NCs. The ring patterns with four measured interplanar spacings are consistent with a face-centered-cubic unit cell, specifically, γ-Al$_2$O$_3$ (space group $Fd\overline{3}m$) instead of Y$_2$O$_3$ (space group $Ia\overline{3}$). Furthermore,
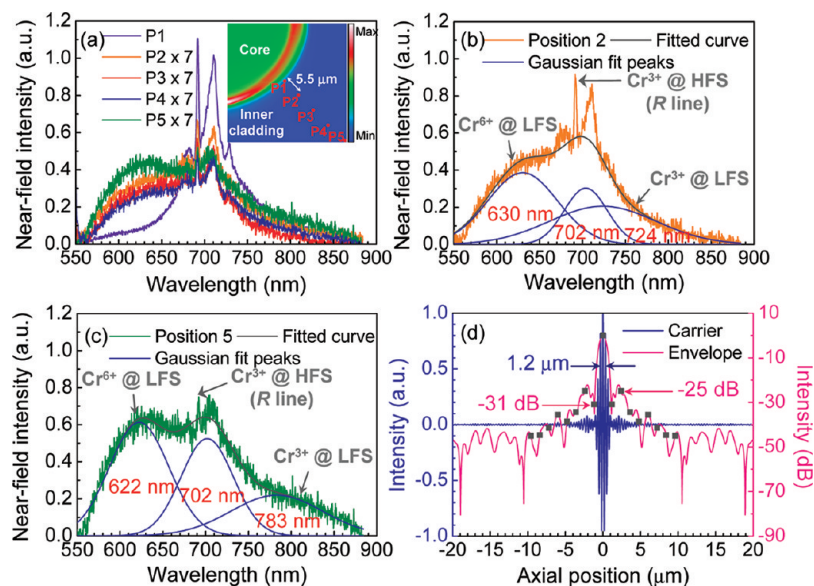
Figure 3. (a) Near-field broadband spectra with sharp R lines obtained in different positions of the CDF inner cladding, with an inset showing the corresponding near-field mapping. (b,c) Multipeak Gaussian fittings of positions 2 and 5, showing an assembly of Cr^{3+} in HFSs (γ-Al_2O_3 NCs) and Cr^{6+} in LHSs (SiO_2 matrixes). (d) Predicted axial resolution in air estimated from part c is around 1.2 μm, accompanied by the power spectrum shown by the pink curve, demonstrating that the low image crosstalks of plus/minus first and plus/minus second pixels are approximately -25 and -31 dB, respectively.

γ-Al_2O_3 NCs were also observed during diffusion bonding of Ni_3Al and alumina—silica fiber.[22] To provide convincing statistics, over 100 NCs were carefully examined. It was found that γ-Al_2O_3 NCs with nanotwinnings comprise ~10% near the core/inner-clad interface. This can be explained by the fact that twinning defects have a high surface energy, thereby indicating that the TB within the NCs is unstable and that the growth rate of twinned NCs is quite low.

3.2. Nanostructure away from the Core/Inner-Clad Interface. To further understand the NC evolution in the radial direction of the CDF, the interior of the inner cladding was also examined in detail. Figure 2a clearly shows a micrometer-sized γ-Al_2O_3 cluster formed away from the CDF core (darker area). A magnified HRTEM image of the cluster is shown in Figure 2c. As confirmed by the line-scan EDX analysis in Figure 2b, the area bounded by red dashed lines has an Al-rich composition. In addition, the sharp-contrast ring SAED pattern in Figure 2d taken from Figure 2c is strong evidence of a crystallized γ-Al_2O_3 cluster. This cluster contains randomly oriented NCs with large sizes and uneven shapes, in which the irregular shapes of the clusters represent the coalescence of neighboring small NCs. The coalescence was forced by the local strain fields due to rapid cooling during the CDLHPG process. This process has been referred to as coarsening by "grain-rotation-induced grain coalescence",[23] leading to a coherent NC/NC plane by eliminating common boundaries, thereby forming a larger single NC as large as 40 nm (marked by arrows in Figure 2c). Farther from the core/inner-clad interface, it was found that the density of γ-Al_2O_3 NCs significantly decreased with increasing SiO_2 matrix concentration. Higher SiO_2 content means that more time is needed to transform into individual NCs with untwined stable structures having lower surface energy. At this point, the twinned NCs comprise only ~2% of the total. Note that there might have been twinned NCs that could not be observed by electron microscopy. Therefore, 2% only sets the lower limit. Figure 2e

shows a representative HRTEM image of a nanotwinned γ-Al_2O_3 NC, accompanied by the corresponding nanobeam SAED pattern viewed along the [011] zone axis, as shown in Figure 2f. Analogous to the face-centered-cubic metal crystallite case,[24−26] this result clearly indicates that the 10-nm-sized γ-Al_2O_3 NC was twinned with a coherent (111) plane, which served as a temporary boundary to reduce the overall surface energy of the adjacent smaller NCs.

3.3. Relationship between Near-Field Spectroscopy and the Nanostructure. To fully correlate the nanostructure with the nanospectroscopy of the γ-Al_2O_3 NCs and clusters, systematic spatially resolved near-field spectroscopy was carried out. Figure 3 shows the near-field spectra of the inner cladding of the CDF. The corresponding near-field mapping is shown in the inset of Figure 3a. The spectra show the broadband properties and their bandwidth and intensity, which are of concern for a potential OCT light source, and these spectra present the dependence on the radial distributions of Cr^{3+}:γ-Al_2O_3 NCs and clusters, as addressed in the following discussion. At position 1 (core/inner-clad interface), a sharp R line (692 nm; $^2E{\rightarrow}^4A_2$ transition) with three phonon sidebands (681, 710, and 728 nm) can be seen, resulting from the Stokes effect, similar to that of ruby crystal.[27] This can be attributed to the Cr ions occupying the high-field sites (HFSs), that is, in association with the octahedral oxygen-coordinated Cr^{3+}, as identified by the HRTEM images of Cr^{3+}:γ-Al_2O_3 NCs in Figure 1e,g. In addition to the HFS emissions, in positions 2−5, Cr^{3+} ions experience a large range of crystal fields in the glass matrix, and hence, the spectra present mixed emissions from the $^4T_2$ level of Cr^{3+} in low-field sites (LFSs). This electronic−vibrational band results in the typical signature of a broadband emission from $^4T_2 \rightarrow ^4A_2$ at ~700−780 nm, as indicated by the multi-Gaussian fittings in Figure 3b,c. This can be attributed to the cluster centers of Cr^{3+} ions. Additionally, positions 2−5 are similar to position 1 with HFS emissions, except that there is an emergence of an emission

band at ∼625 nm due to the formation of Cr^{6+} in SiO_2 matrix with tetrahedral packaging of oxygens.[28,29] Actually, based on the compiled effective ionic radii, Cr^{6+} (0.026 nm) has a compatible ionic size to Si^{4+} (0.026 nm) in coordination number 4 of the silicate framework.[30] In addition, the emission band of Cr^{3+}: Y_2O_3 centered at 660 nm[31] differs from the measured near-field spectrum of Cr^{3+}:γ-Al_2O_3 (∼625 nm in Figure 3). Therefore, the growth of Y_2O_3 clusters and Cr^{3+}:Y_2O_3 luminescence can be excluded in the CDF.

However, it should be noted that the main difference between positions 2 and 5 is that the $^2E \rightarrow ^4A_2$ R-line emission exhibits a much stronger intensity from position 2 than from position 5. The stronger R-line transition rate indicates that there is a large fraction of Cr ions in HFSs, whereas a majority of Cr ions occupy the LFSs at position 5. This observation agrees well with the fact that the amount of SiO_2 matrixes increases and the density of γ-Al_2O_3 NCs decreases as one moves away from the core/inner-clad interface. Moreover, the peak intensities of Cr^{3+} and Cr^{6+} show an opposite correlation (i.e., R line versus 625-nm emission), suggesting that the contents of Cr^{3+} and Cr^{6+} vary systematically with basicity, which is in accordance with the Cr^{3+}–Cr^{6+} redox reaction in silicate glass.[29] Because there are many possible oxidation states for Cr ion in glass, it has been shown in the literature that basicity can affect Cr ion oxidation.[32] The basicity of the fiber varies with glass composition. In fact, position-dependent variation of the major contents of Al_2O_3, Y_2O_3, and SiO_2 was found throughout the inner cladding of the CDF by electron probe microanalysis (EPMA). The varied compositions mainly stem from the interdiffusion process. This means that the basicity of this alumino-silicate cladding changes with varied glass compositions. Another important feature that can be observed from positions 2–5 is that the entire broadband emission intensity has dropped by a factor of 7 compared with that obtained in position 1. The decrease in Cr emission can be attributed to the decrease of both the Cr content and the Cr emission cross section. However, the latter should be the key factor because the EPMA measurement indicated quite a uniform Cr ion concentration (∼0.1 wt %) throughout the inner cladding. This result indicates that planar defects could begin to occur in these positions, which is consistent with the above HRTEM observations showing that nanotwinnings and micro-sized clusters play key roles in determining optical properties (Figures 1 and 2).

3.4. Crystal-Fiber-Based Broadband Emission for High-Axial-Resolution OCT. More importantly, the 165-nm 3-dB bandwidth centered at 690 nm reveals the potential for this to be a high-axial-resolution OCT light source, as shown in Figure 3c. To demonstrate this, Figure 3d shows the stimulated interferometric signal using the broadband spectrum taken in position 5. The predicted axial resolution in air estimated from the 165-nm 3-dB bandwidth is around 1.2 μm, smaller than those of OCTs based on Ti^{3+}:sapphire (2.2 μm) and Ce^{3+}:YAG (1.5 μm).[33,34] According to this 1.2-μm axial resolution and to further quantitatively evaluate the crosstalk level that deteriorates the image quality through image pixel crosstalk, the normalized power envelope $20 \log[H(z)]$ was calculated using the Hilbert transform, $H(z)$, of the stimulated interferometric signal, as shown by the pink curve in Figure 3d. The pixel indicator in Figure 3d was marked at the center of each pixel, and the pixel size has 1.2-μm axial resolution, indicating that the crosstalk of the plus/minus first and plus/minus second pixels of the broadband emission in the CDF is about −25 and −31 dB, respectively.

These results demonstrate the superiority of the CDF broadband emission in terms of both axial image crosstalk and high axial resolution.

4. CONCLUSIONS

In conclusion, a plausible explanation for the twinned and single larger γ-Al_2O_3 NC formation mechanism was proposed. The NC distribution and local environment of the emitters were shown to have a significant impact on the broadband emission from CDFs grown by the CDLHPG technique. Twinned NCs were generated by interdiffusion followed by high-temperature annealing and rapid cooling. Our observations are consistent with crystal-field ligands. In addition, nanospectroscopy of the 165-nm broadband emission was shown to result from an assembly of Cr^{3+} in HFSs (γ-Al_2O_3 NCs) and Cr^{6+} in LHSs (SiO_2 matrix), providing 1.2-μm axial resolution in air for OCT. Based on the nanostructural and nanospectroscopic results, this study provides a concept for tailoring broadband emission in CDFs for high-axial-resolution OCT applications.

■ ASSOCIATED CONTENT

Ⓢ Supporting Information. Description of the multipump near-field scanning optical microscope (NSOM). This information is available free of charge via the Internet at http://pubs.acs.org.

■ AUTHOR INFORMATION

Corresponding Author
*E-mail: slhuang@cc.ee.ntu.edu.tw.

■ ACKNOWLEDGMENT

■ REFERENCES

(1) Huang, D.; Swanson, E. A.; Lin, C. P.; Schuman, J. S.; Stinson, W. G.; Chang, W.; Hee, M. R.; Flotte, T.; Gregory, K.; Puliafito, C. A.; Fujimoto, J. G. *Science* **1991**, *254*, 1178.

(2) Wang, R. K. *Appl. Phys. Lett.* **2007**, *90*, 054103–1.

(3) Tearney, G. J.; Brezinski, M. E.; Bouma, B. E.; Boppart, S. A.; Pitris, C.; Southern, J. F; Fujimoto, J. G. *Science* **1997**, *276*, 2037.

(4) Drexler, W.; Morgner, U.; Kärtner, F. X.; Pitris, C.; Boppart, S. A.; Li, X. D.; Ippen, E. P.; Fujimoto, J. G. *Opt. Lett.* **1999**, *24*, 1221.

(5) Alivisatos, A. P. *Science* **1996**, *271*, 933.

(6) Mercier, B.; Ledoux, G.; Dujardin, C.; Nicolas, D.; Masenelli, B.; Mélinon, P.; Bergeret, G. *J. Chem. Phys.* **2007**, *126*, 044507.

(7) Mercier, B.; Dujardin, C.; Ledoux, G.; Nicolas, D.; Masenelli, B.; Mélinon, P. *J. Lumin.* **2007**, *122–123*, 756.

(8) Lai, C. C.; Ke, C. P.; Liu, S. K.; Jheng, D. Y.; Wang, D. J.; Chen, M. Y.; Li, Y. S.; Yeh, P. S.; Huang, S. L. *Opt. Lett.* **2011**, *36*, 784.

(9) Pan, C.; Chen, S. Y.; Shen, P. *J. Phys. Chem. B* **2006**, *110*, 24340.

(10) Berg, O.; Hamdy, M. S.; Maschmeyer, T.; Moulijn, J. A.; Bonn, M.; Mul, G. *J. Phys. Chem. C* **2008**, *112*, 5471.

(11) Wang, D.; Xing, G.; Peng, H.; Wu, T. *J. Phys. Chem. C* **2009**, *113*, 7065.

(12) Zhou, S.; Antonietti, M.; Niederberger, M. *Small* **2007**, *3*, 763.

(13) McHale, J. M.; Auroux, A.; Perrotta, A. J.; Navrotsky, A. *Science* **1997**, *277*, 788.

20293

dx.doi.org/10.1021/jp203901t |*J. Phys. Chem. C* 2011, 115, 20289–20294

(14) Sakate, H.; Sakuma, F.; Ono, A. *Metrologia* **1995**, *32*, 129.

(15) HcHale, J. M.; Navrotsky, A.; Perrotta, A. J. *J. Phys. Chem. B* **1997**, *101*, 603.

(16) *NIST Thermochemical Tables*; National Institute of Standards and Technology (NIST): Gaithersburg, MD, 1985, p 158.

(17) Chryssolouris, G. *Laser Machining: Theory and Practice*; Springer: New York, 1991; p 274.

(18) Chrisey, D. B.; Hubler, G. K. *Pulsed Laser Deposition of Thin Films*; John Wiley & Sons: New York, 1994; p 613.

(19) Incropera, F. P.; DeWitt, D. P. *Fundamentals of Heat and Mass Transfer*; John Wiley & Sons: New York, 2002; p 930.

(20) Kasap, S. O. *Principles of Electronic Materials and Devices*; McGraw-Hill: New York, 2004; p 155.

(21) Chen, S. Y.; Shen, P. *Phys. Rev. Lett.* **2002**, *89*, 096106–1.

(22) Hu, W.; Gottstein, G. *Mater. Sci. Eng. A* **2002**, *338*, 313.

(23) Leite, E. R.; Giraldi, T. R.; Pontes, F. M.; Longo, E.; Beltrán, A.; Andrés, J. *Appl. Phys. Lett.* **2003**, *83*, 1566.

(24) Xu, L.; Su, Y.; Chen, Y.; Xiao, H.; Zhu, L.; Zhou, Q.; Li, S. *J. Phys. Chem. B* **2006**, *110*, 6637.

(25) Maksimuk, S; Teng, X.; Yang, H. *J. Phys. Chem. C* **2007**, *111*, 14312.

(26) Ma, Y.; Jiang, Z.; Kuang, Q.; Zhang, S.; Xie, Z.; Huang, R.; Zheng, L. *J. Phys. Chem. C* **2008**, *112*, 13405.

(27) Ribeiro, C. T. M.; Zanatta, A. R. *Appl. Phys. Lett.* **2003**, *83*, 2336.

(28) Stręk, W.; Dereń, P. J.; Łukowiak, E.; Hanuza, J.; Drulis, H.; Bednarkiewicz, A.; Gaishun, V. *J. Non-Cryst. Solids* **2001**, *288*, 56.

(29) Murata, T.; Torisaka, M.; Takebe, H.; Morinaga, K. *J. Non-Cryst. Solids* **1997**, *220*, 139.

(30) Shannon, R. D. *Acta Crystallogr. A* **1976**, *32*, 751.

(31) Schaik, W. V.; Blasse, G. *Chem. Mater.* **1992**, *4*, 410.

(32) Suzuki, Y.; Kawasaki, S.; Ookawa, M.; Yokokawa, T. *Mater. Trans.* **1995**, *36*, 1483.

(33) Kowalevicz, A. M.; Ko, T.; Hartl, I.; Fujimoto, J. G.; Pollnau, M.; Salathé, R. P. *Opt. Express* **2002**, *10*, 349.

(34) Tsai, C. C.; Chen, T. H.; Lin, Y. S.; Wang, Y. T.; Chang, W.; Hsu, K. Y.; Chang, Y. H.; Hsu, P. K.; Jheng, D. Y.; Huang, K. Y.; Sun, E.; Huang, S. L. *Opt. Lett.* **2010**, *35*, 811.

20294

dx.doi.org/10.1021/jp203901t |*J. Phys. Chem. C* 2011, 115, 20289–20294